Watermass co-ordinates isolate the historical climate change signal

T. Sohail[a,b] , R. M. Holmes[c] and J.D. Zika[a,b,d]

[a] *School of Mathematics and Statistics, University of New South Wales, Sydney, Australia*

[b] *Australian Centre for Excellence in Antarctic Science (ACEAS), University of New South Wales, NSW, Australia*

[c] *School of Geosciences, University of Sydney, Sydney, Australia*

[d] *UNSW Data Science Hub, University of New South Wales, Sydney, Australia*

Corresponding author: Taimoor Sohail, t.sohail@unsw.edu.au

ABSTRACT: Persistent warming and water cycle change due to anthropogenic climate change modifies the temperature and salinity distribution of the ocean over time. This 'forced' signal of temperature and salinity change is often masked by the background internal variability of the climate system. Analysing temperature and salinity change in watermass-based coordinate systems has been proposed as an alternative to traditional Eulerian (e.g., fixed-depth, zonally-averaged) co-ordinate systems. The impact of internal variability is thought to be reduced in watermass co-ordinates, enabling a cleaner separation of the forced signal from background variability - or a higher 'signal-to-noise' ratio. Building on previous analyses comparing Eulerian and watermass-based one-dimensional coordinates, here we recast two-dimensional co-ordinate systems - temperature-salinity ($T-S$), latitude-longitude and latitude-depth - onto a directly comparable equal-volume framework. We compare the internal variability, or 'noise' in temperature and salinity between these remapped two-dimensional co-ordinate systems in a 500 year pre-industrial control run from a CMIP6 climate model. We find that median internal variability is reduced in both ocean heat and salt content in $T-S$ space compared to Eulerian coordinates, and that a large proportion of variability in $T-S$ space can be attributed to processes which operate over a timescale greater than 10 years. We show that, as a consequence of the reduced projection of internal variability into $T-S$ space, the signal-to-noise ratio in watermass co-ordinates is at least two times greater than in Eulerian co-ordinate systems, implying that the climate change signal can be more robustly identified.

SIGNIFICANCE STATEMENT: Changes in ocean temperature and salinity are driven both by human-induced climate change and by modes of natural variability in the climate system, such as the El-Niño Southern Oscillation. It can be difficult to isolate the human-induced 'signal' of climate change from the natural fluctuations or 'noise' in the climate system. Watermass-based methods, which 'follow' a parcel of water around the ocean, have been thought to improve on 'Eulerian' (i.e., analyses performed at fixed latitude, longitude and depth) frames of reference as they are less impacted by the 'noise'. However, it is difficult to cleanly compare between watermass-based methods and Eulerian methods. Here, we aim to quantify the extent to which watermass-based frameworks improve on Eulerian frameworks in isolating the climate signal from the noise. We recast watermass and Eulerian methods onto an equivalent grid, enabling a clean comparison between them, and find that doing so reduces the median signal-to-noise ratio in watermass-based co-ordinates by a factor of at least two. These results emphasise the utility of watermass-based methods in analysing long-term climatic changes in the ocean.

1. Introduction

Anthropogenic climate change is characterised by the persistent build-up of heat in the climate system (Stocker et al. 2013) and long-term changes to the hydrological cycle (Durack et al. 2012; Sohail et al. 2022). A vast proportion of excess heat in the climate system is absorbed by the ocean (Schuckmann et al. 2020), and changes to the water cycle manifest as ocean salinity changes (Pierce et al. 2012). These human-induced changes to ocean heat and salinity occur alongside natural variability in the climate system, driven in part by physical modes of climate variability like the El-Niño Southern Oscillation (ENSO) (Trenberth 2020) and the North Atlantic Oscillation (Visbeck et al. 2001). Natural variability in the climate system can obscure forced anthropogenic trends in the ocean, adding 'noise' to the system that can obscure the signal.

Numerous studies have aimed to tackle the problem of detecting the anthropogenic signal of climate change in observations and climate models. A conventional approach to detecting changes in ocean temperature and/or salinity involves detecting changes to ocean properties at fixed locations on the ocean surface (that is, in latitude-longitude co-ordinates, Hawkins and Sutton 2012; Hamlington et al. 2011) or by zonally-averaging (that is, in latitude-depth co-ordinates, Pierce et al. 2012; Silvy et al. 2020; Boyer et al. 2005). In these traditional Eulerian frames of reference, the

'noise', natural variability in the climate system, can be reduced by coarsening the grid, filtering out the relevant time-scales, taking large ensemble means, and/or by focusing on specific ocean regions that may not be impacted by dominant modes of variability (Hamlington et al. 2011; Penland and Matrosova 2006; Maher et al. 2021; Pierce et al. 2012). In doing so, this past research has effectively increased the 'signal-to-noise' ratio - allowing for a more robust identification of the long-term climate change-induced trend.

Watermass-based frameworks have been proposed as an alternative to traditional Eulerian-based methods for tracking ocean change. Tracking changes in ocean properties following iso-surfaces of conservative tracers, such as density, temperature and/or salinity, is thought to filter out short-timescale, highly variable adiabatic motions, potentially reducing internal variability and noise in the system (Silvy et al. (2020); Palmer et al. (2007); Zika et al. (2015, 2021)). In addition, watermass-based methods can enable a direct attribution of heat or salt content tendencies to surface fluxes and diabatic mixing, as only diabatic flux terms are present in the budget (Walin 1982; Groeskamp et al. 2019; Holmes et al. 2019; Bladwell et al. 2021; Hieronymus et al. 2014).

However, a clean comparison of the internal variability, and thus signal-to-noise ratio, in watermass-based and Eulerian methods is challenging because the volume bounded by watermass-based coordinate surfaces can change with time. Thus, a given temperature or salinity surface could expand to fill a large portion of the ocean, while volumes bounded by latitude, longitude and depth surfaces are (by construction) fixed in time. For instance, Palmer et al. (2007); Palmer and Haines (2009) compared ocean temperature variability above the $14°C$ isotherm, and the 220m depth level, which are approximately geographically collocated. While the use of a temperature-based co-ordinate reduces internal variability, the $14°C$ isotherm expands over time to accommodate an increasingly warm ocean, while the 220m depth level remains fixed. Following work by Sohail et al. (2021), Holmes et al. (2022) avoided this problem by using a percentile-based co-ordinate system that enables a constant-volume comparison between one-dimensional temperature, depth and latitude co-ordinate systems. Holmes et al. (2022) showed that internal variability is indeed reduced in one-dimensional temperature co-ordinates (aligning with findings from Palmer and Haines (2009)), but only for specific timescales and regions of the ocean.

While one-dimensional fixed-depth and fixed-temperature frameworks remain popular choices in assessing ocean heat and salt content (Wolfe et al. 2008; Morrison and Hogg 2013; Sohail et al.

2021, 2022), two-dimensional co-ordinate systems retain more information and are often used to assess ocean heat and salt content change (e.g., Roemmich et al. (2015); Silvy et al. (2020); Rathore et al. (2020)). For instance, in one dimension, 'cold' temperature surfaces conflate the ocean interior with surface polar regions, but introducing a second dimension (e.g. salinity) isolates the interior ocean from the polar surface effectively. Variability in two-dimensional watermass coordinates has been compared to variability in Eulerian coordinates by 're-projecting' diabatic tendencies inferred in water mass coordinates back onto the geographical coordinates. Evans et al. (2014) inferred seasonal diabatic tendencies in $T-S$ coordinates within Drake's Passage and then remapped these onto the average locations of the corresponding $T-S$ classes along a repeat hydrographic section. Similarly, Zika et al. (2021) inferred diabatic tendencies necessary to explain changes in the global inventories of sea water in $T-S$ coordinates and mapped these onto the 3D geographical distribution of those water masses. In each case, Eulerian changes were larger than the inferred diabatic tendencies. However, these methods have relied on inferring the diabatic tendency from either a numerical model or an inverse model, and the derived solution is not necessarily unique. Thus, a clean, objective comparison assessing whether the projection of internal variabilty into two-dimensional watermass frameworks (e.g. Temperature versus Salinity, hereafter $T-S$ co-ordinates) is reduced compared to Eulerian counterparts (e.g., latitude-longitude, latitude-depth) has not been conducted.

In this paper, we recast two dimensional co-ordinate systems, namely, $T-S$ space, latitude-longitude space, and latitude-depth space, onto a constant-volume-based two-dimensional framework using a statistical method called *Binary Space Partitioning* (BSP). We then track changes to the ocean's temperature and salinity properties to quantify internal variability (the 'noise') with the aim of establishing whether the median internal variability is reduced in watermass-based frameworks leading to an increased signal-to-noise ratio of the climate signal. The coupled climate model data used in this study is described in section 2. We provide details of BSP and its two-dimensional remapping in section 3. Our findings, detailed in section 4, confirm that not only is the median internal variability (the 'noise') significantly reduced in $T-S$ space, it is described by longer timescale processes, and by fewer statistical modes. We explore the historical 'signal' in section 5, and show that the median signal-to-noise ratio is at least two times larger in $T-S$ space compared to its Eulerian counterparts. Conclusions are summarised in section 6.

2. Model data: ACCESS-CM2

In this work, we focus on a number of simulations performed using the ACCESS-CM2 climate model (Bi et al. 2020) as part of the Australian submission to the 6th generation Climate Model Intercomparison Project (CMIP6) (Eyring et al. 2016). The ocean model component of ACCESS-CM2 is the Modular Ocean Model version 5.1 (Griffies 2012) which uses Conservative Temperature and Practical Salinity as its standard temperature (T) and salinity (S) variables (McDougall 2003; McDougall and Barker 2011). More details on ACCESS-CM2, the ACCESS-CM2 submission to CMIP6, and in particular, the forcing and spin-up of the piControl and historical runs, are provided by Bi et al. (2020).

We analyse a 500 year pre-industrial control (piControl) simulation, as well as a 165 year historical simulation (Eyring et al. 2016). In this work, we analyse the model Conservative Temperature, Practical Salinity and grid cell volume variables in temperature-salinity, latitude-longitude, and latitude-depth coordinates over the entire pre-industrial control period. We also analyse the model Potential Temperature, Practical Salinity and grid cell volume variables over the entire historical period, covering 1850 to 2014.

The monthly-averaged temperature and salinity in the piControl and historical runs are first binned into 2D $T-S$, latitude-longitude and latitude-depth percentile coordinates using BSP as described in section 3. Binned outputs are then de-drifted and de-seasoned prior to analysis. De-drifting is accomplished by removing a cubic fit of the piControl time series over the relevant overlapping time period, following Irving et al. (2020). The seasonal cycle is removed by subtracting the time-mean seasonal cycle over the entire time period of interest from the monthly time series.

3. Theory

Typically, watermass-based analyses involve tracking ocean properties at constant temperature or salinity (Worthington 1981; Walin 1982; Zika et al. 2015, 2018; Holmes et al. 2019). By following constant tracer isosurfaces, the heat and salt budgets contain contributions from diabatic processes only. However, there are still diasurface volume fluxes in these coordinates which must be accounted for and whose associated tracer flux may be ill-defined (see Holmes et al. (2019) and Bladwell et al. (2021) for details). In addition, as the surface outcrop location of temperature and salinity surfaces may shift over time, it is difficult to link changes at a given tracer isosurface to a

specific geographical region in strongly forced ocean models. Thus, cleanly comparing between pure watermass-based coordinate systems and Eulerian coordinate systems (which track ocean changes at fixed latitude, longitude or depth) can be difficult, in part because Eulerian coordinate systems are fixed-volume by construction, while the volume of water bounded by temperature or salinity surfaces can change with time.

a. Binary Space Partitioning

In order to overcome this issue, we recast all 2D co-ordinate systems using a statistical method called Binary Space Partitioning (BSP). Originating from computer graphics and image processing fields (e.g. Radha et al. (1996); Thibault and Naylor (1987)), BSP is a method for recursively, hierarchically subdividing a distribution using arbitrarily oriented lines. We can use BSP to effectively partition the ocean's two-dimensional volume distribution into equal weight bins in watermass and Eulerian space.

To illustrate how BSP works, consider a two-dimensional volume distribution $v(x, y)$ which is the volume of sea-water per unit x and y. x and y can be coordinates defined by Eulerian space or coordinates defined by time variable scalars such as T, S, density, etc. To form a BSP tree, we recursively subdivide the distribution with alternating axis-oriented lines n times, such that the volume of the ocean in each subdivision is $1/2^n$ of the total ocean volume $\iint v(x, y)dxdy$. This procedure is shown graphically in Figure 1.

The initial slice (figure 1a) divides the volume in half along some $y-$value y_1, such that each subdivision contains half of the ocean volume $\frac{1}{2}\iint v(x, y)dxdy$. The subsequent slice (figure 1b) divides each subdivided section further in half along two $x-$values x_1 and x_2, such that each subdivision now contains a quarter of the ocean volume, $\frac{1}{4}\iint v(x, y)dxdy$. This process of recursive subdivision is repeated n times along alternating axes such that each time a volume constraint of $\frac{1}{2^n}\iint v(x, y)dxdy$ is met. The resulting BSP tree structure thus compresses any general distribution into equal-volume bins.

Once the BSP has been performed for a given choice of x and y coordinates, we can track changes to the mean temperature, T and salinity, S in each bin over time. This allows us to quantify how variability ('noise') behaves in each co-ordinate system regardless of whether it is Eulerian or water-mass based.

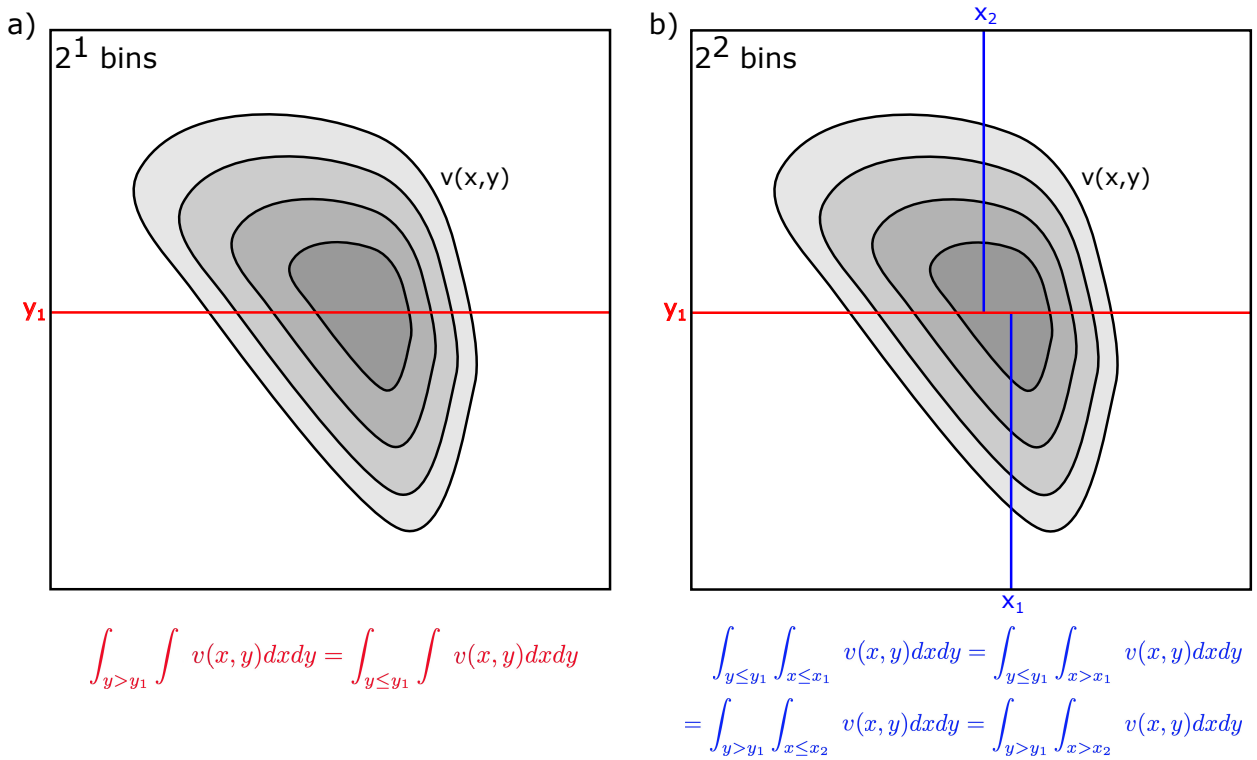

FIG. 1. A simple demonstration of Binary Space Partitioning applied to a generic two-dimensional volume distribution. a) One slice orthogonal to the y-axis at y_1 (in red) yields 2^1 equal-volume bins of $v(x,y)$. b) Two additional slices orthogonal to the x-axis at x_1, x_2 (in blue) yield 2^2 equal-volume bins of $v(x,y)$.

In this work, we use BSP to partition the ocean's volume into 2^n equal-volume bins in three 2D coordinate systems: $T-S$, latitude-longitude and latitude-depth space. We first illustrate the partitioning of the ocean's $T-S$ volume distribution in the ACCESS-CM2 piControl run in figure 2 for $n = 1, 2, 5$, and 8.

In latitude-longitude and latitude-depth co-ordinates, we perform BSP on the depth-integrated and zonally-integrated volume distribution, respectively. To account for the periodicity of longitude, we choose to ensure that the Americas and Drake Passage form both the far western and far eastern boundary of the ocean. This is done by slicing the ocean at $70°W$ longitude from $90°S$ to $3°N$ latitude, then a diagonal slice is made from $70°W$ longitude to $100°W$ between $3°N$ latitude and $20°N$, and the slice continues north from $20°N$ to $90°N$ along the $100°W$ longitude. Data points between this line and the Greenwich Meridian, moving east, are labelled with negative longitudes (i.e. are measured west of Greenwich) while the remaining data points to the east of Greenwich are

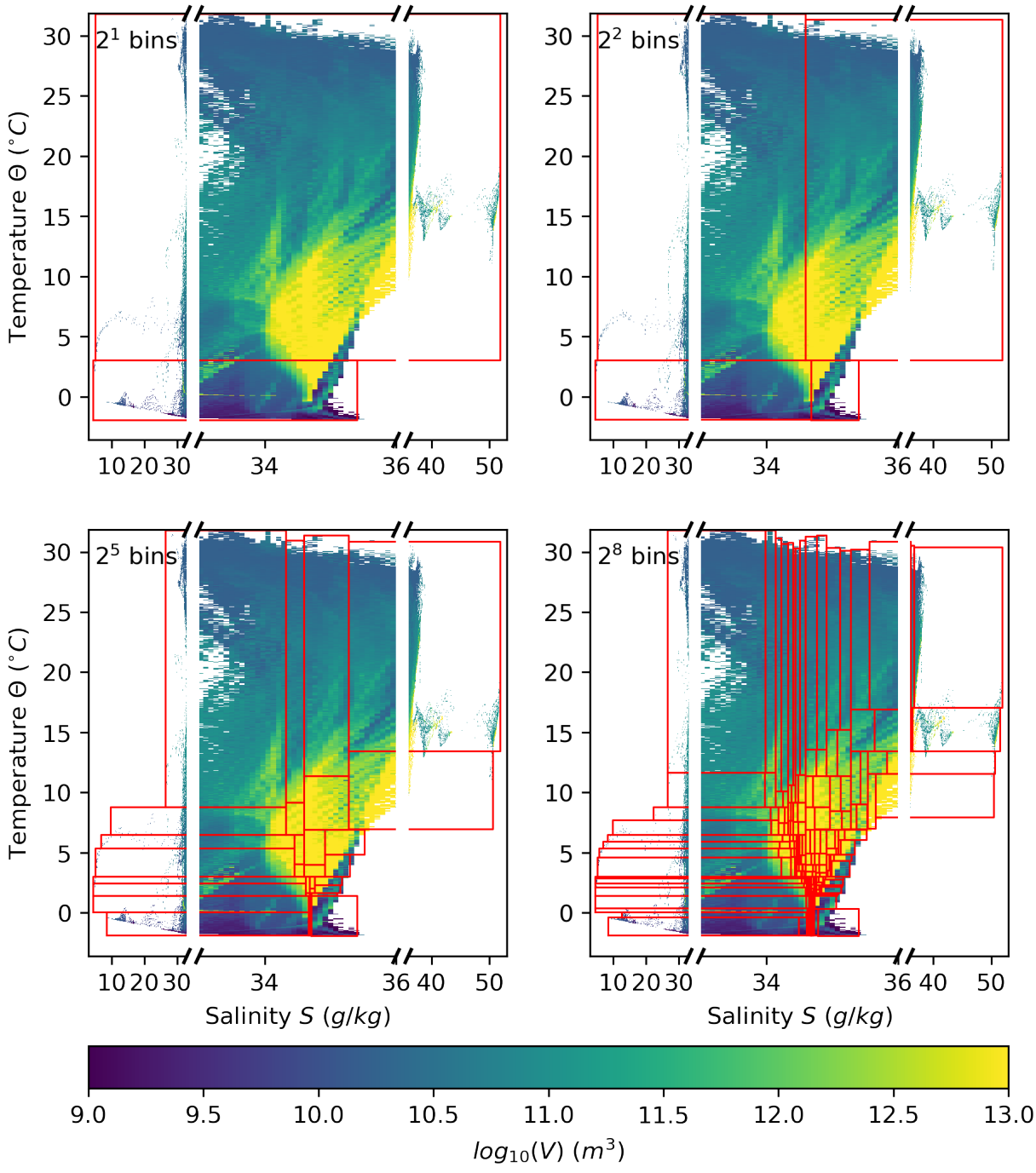

FIG. 2. BSP splitting on alternating axes, applied to the ACCESS-CM2 piControl volumetric distribution in $T-S$ space, with 2^n bins, where a) n=1, b) n=2, c) n=5, and d) n=8. Note that the salinity axis has three linear scales, delineated by the two horizontal breaks.

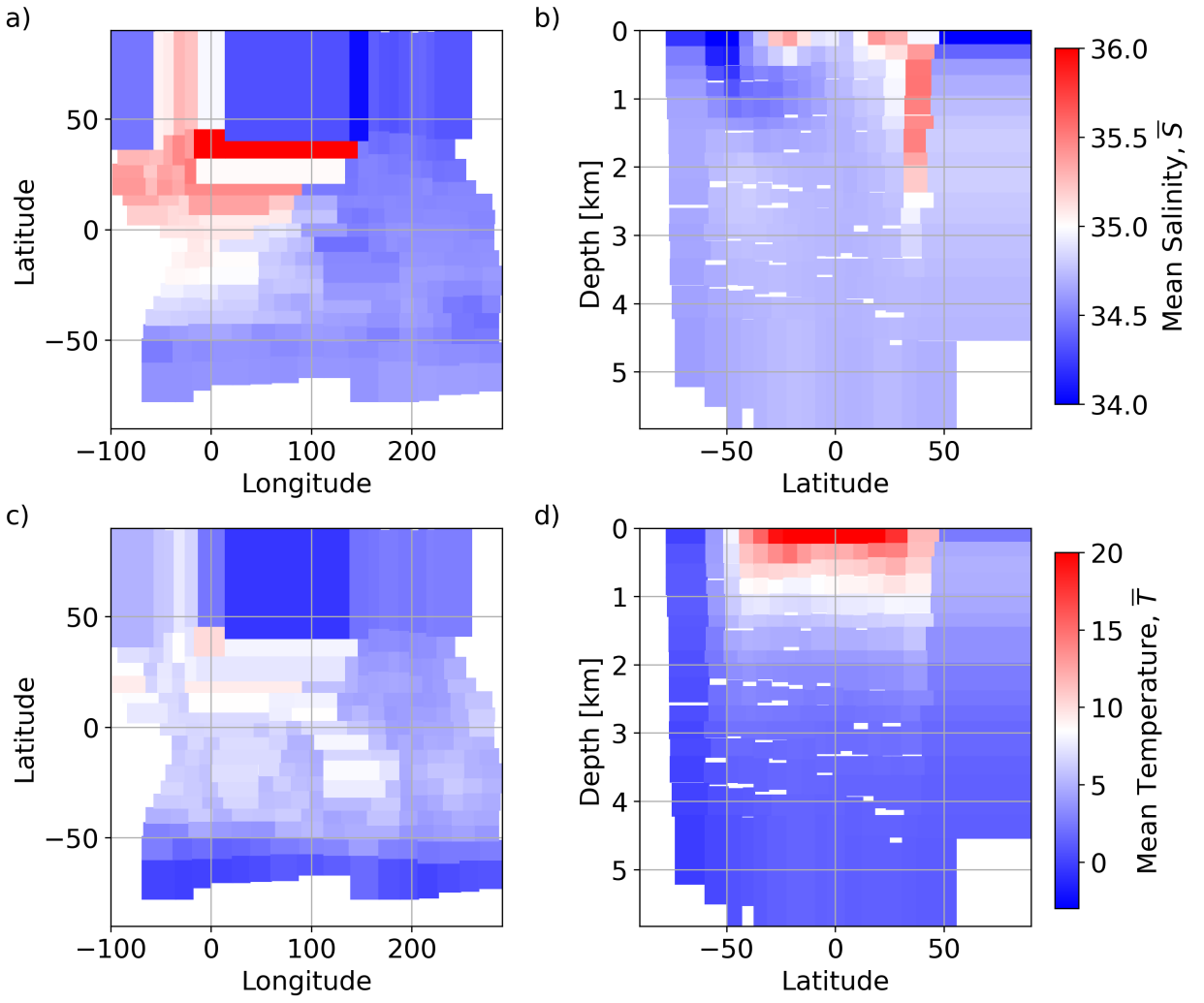

FIG. 3. BSP splitting on alternating axes with 2^8 bins, applied to the ACCESS-CM2 piControl (a and c) depth-integrated volumetric distribution in latitude-longitude co-ordinates, and (b and d) zonally-integrated volumetric distribution in latitude-depth co-ordinates. BSP bins are coloured by the time-mean (top row) salinity and (bottom row) temperature in each bin.

labeled with positive longitudes (i.e. are measured east of Greenwich). This ensures, for example, that data points either side of the Isthmus of Panama do not combine into the same BSP bin. Figure 3 shows the resulting BSP bins in both Eulerian co-ordinate systems for $n = 8$, coloured by their mean temperature and salinity.

Note that in BSP, the choice of which axis to cut along, or indeed the angle of the line that makes the cut, is entirely arbitrary. If choosing to cut orthogonal to the distribution axes, there

exist 2^n combinations of the order of subdivision that are valid. More generally, the choice to slice orthogonally to an axis is also arbitrary, and the BSP algorithm could, for instance, be directed to modify its angle until the volume constraint $\frac{1}{2^n}\iint v(x,y)dxdy$ is met. That said, not all combinations are physically plausible when subdividing the ocean in $T-S$ or Eulerian space, and we opt to focus hereafter on the specific case of orthogonal slices alternating between the $y-$ and $x-$ axes ($yxyxyxyx$ for 8 cuts). This order of BSP split combinations preserves the aspect ratio of BSP bins, ensuring a more equivalent representation of $x-$ and $y-$ variability. We explore this aspect ratio argument, and impact of choosing to slice along other orders of subdivision, in the Appendix, and reserve exploration of non-orthogonal slices in BSP for future work.

b. Visualising 2D BSP framework

In Eulerian space, the BSP bins generally align with the regular latitude-longitude (or latitude-depth) grid, as demonstrated by the general uniformity in BSP bin size in figure 3. However, in $T-S$ space, the ocean's volume is concentrated over a relatively narrow range of temperatures and salinities (figures 2). Thus, the equal-volume binning using BSP leads to a large difference in the temperature and salinity ranges spanned by a given bin in $T-S$ space. Surface waters (which occupy a large range of temperatures and salinities but represent minimal volume) are over-represented in the visualisation, as exhibited in figure 4a. Instead, it is advantageous to visualise each bin with an equal area in order to more clearly convey the equal-volume nature of the BSP framework. In order to achieve this, we make use of the binary tree structure obtained from the BSP. By construction, the corner bins obtained from the BSP (i.e, the top-right, top-left, bottom-right and bottom-left bins) represent the extrema in $T-S$ space. All other bins are situated relative to these extrema in the BSP tree, and can be remapped relative to these corner bins. Hence, we remap the bins obtained from BSP onto a plot relative to the ocean's extrema.

In figure 4, we plot the output of this remapping in $T-S$ space. We plot the mean salinity (figure 4a and b) and the mean temperature (figure 4c and d) within each BSP bin in $T-S$ and in remapped $T-S$ space. The remapping effectively preserves the fresh-to-salty and hot-to-cold gradient of temperature and salinity in each bin (figure 4b and d). The use of the BSP tree structure in the remapping ensures that each bin (representing a single unit of volume) is saltier (fresher) and hotter (colder) than the bin to its left (right) and below (above) it.

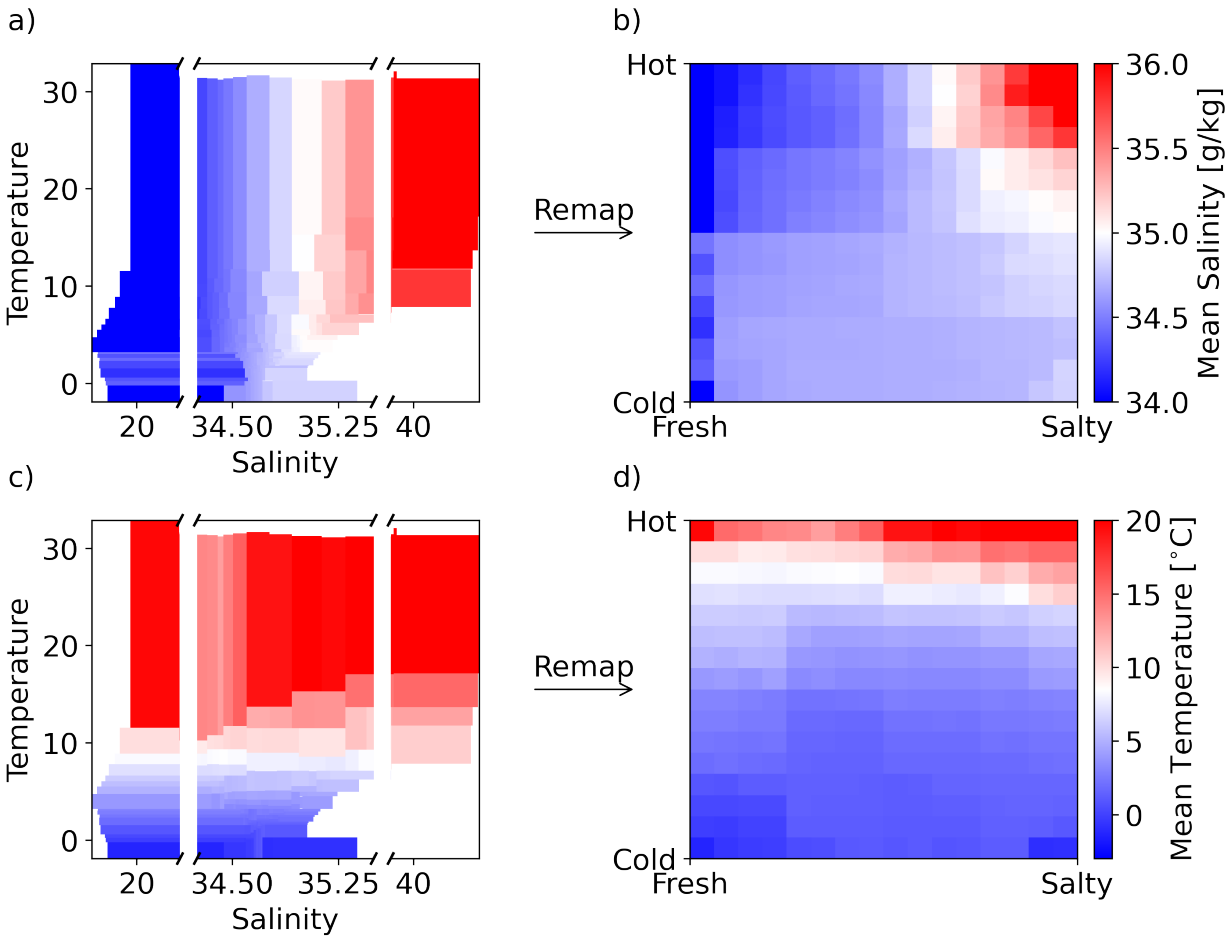

FIG. 4. Remapping BSP bins from (a and c) real $T-S$ space, to (b and d) relative $T-S$ space based on a binary tree structure. BSP bins are coloured by (a and b) time-mean salinity, and (c and d), time-mean temperature in the ACCESS-CM2 piControl run.

The characteristic salinity and temperature of the global ocean can be seen in the remapped BSP plots in all coordinate systems (figure 5). The salty North Atlantic is visible in the top left of figure 5b and right side of figure 5c, while the relatively fresher Pacific and Southern Oceans are evident in the bottom and right hand side of figure 5b and top left of figure 5c, respectively. The clear thermal stratification of the global ocean through depth is also retained in the remapped latitude-depth plots, as shown in figure 5f.

In this work, we present all results in the form of this remapped BSP visualisation, as it provides equal visual weight to each volume of ocean regardless of the space occupied by each bin in its original coordinate system. This remapping also retains the salient features of the different

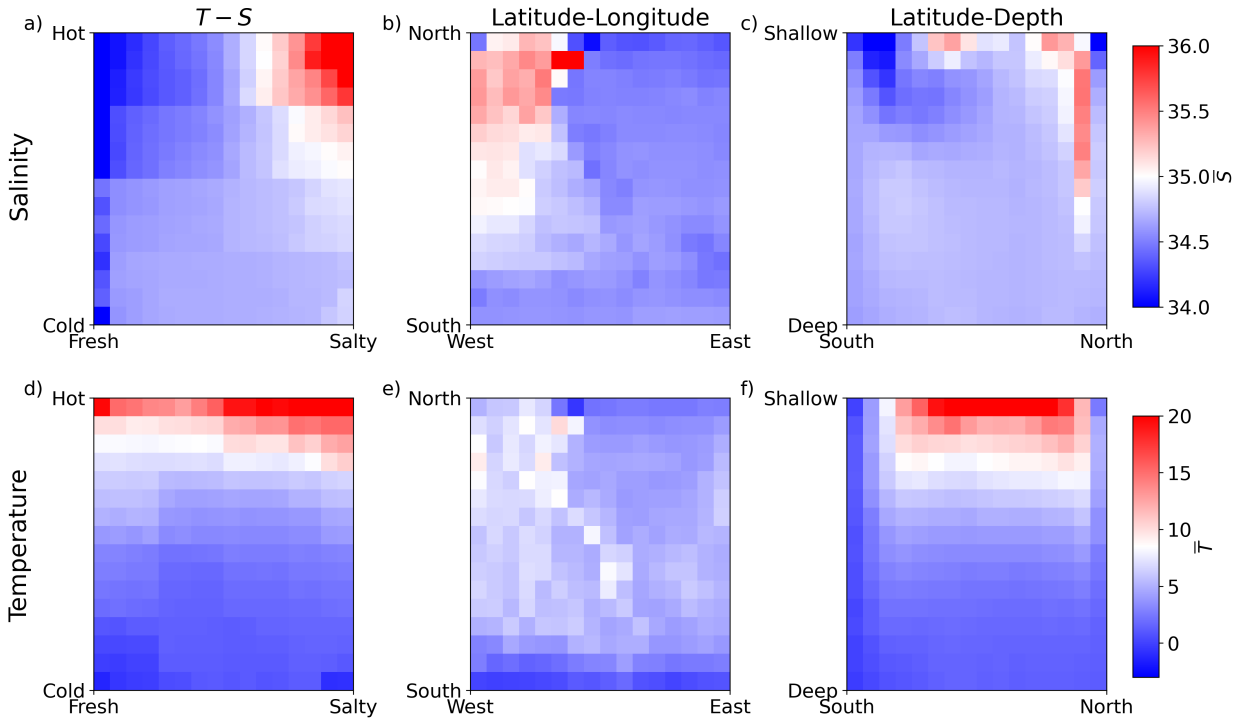

235 FIG. 5. Time-mean (a - c) salinity and (d - f) temperature in remapped equal-volume BSP bins, in (a and d)
236 $T-S$, (b and e) latitude-longitude, and (c and f) latitude-depth co-ordinates, from the ACCESS-CM2 piControl
237 simulation.

247 coordinate systems while presenting the data on an equivalent constant-volume metric, enabling a
248 cleaner comparison between different coordinate systems. For ease of interpretation of the BSP
249 remapping and further results in $T-S$ space, we show the broad geographic distribution of the
250 warmest (coldest), freshest (saltiest) 25% volume of the ocean in the Appendix (figure B1).

251 *c. Signal-to-Noise Ratio*

252 The signal-to-noise ratio is commonly employed to determine the relative impact of internal
253 variability in the climate system (e.g., Hawkins and Sutton (2012)). Here, we define signal-
254 to-noise ratio (F/N) as the change in temperature (or salinity) in a given bin over the historical
255 period (1850 to 2014), divided by the standard deviation of the temperature (or salinity) over the
256 pre-industrial control period:

$$F/N = \Delta C/\sigma_{control}, \tag{1}$$

where C is any generic tracer. In this work, we calculate F/N for the mean T and S in all BSP bins in $T-S$, latitude-longitude, and latitude-depth co-ordinates (section 5).

4. Results

The BSP framework enables an equal-volume comparison between three popular two-dimensional coordinate systems used to assess ocean and climatic changes - the temperature-salinity, latitude-longitude, and latitude-depth coordinate systems. In this section, we explore the internal variability, or 'noise', in these three co-ordinate systems.

a. Internal Variability

We begin by assessing the internal variability in the mean temperature and salinity of each BSP bin in the three coordinate systems in question. Overall, the $T-S$ coordinate system exhibits a broad range in variance, from low variability in BSP bins corresponding to the ocean interior (bottom-middle bins in figure 6a and d), to high variability in BSP bins corresponding to the ocean's surface (edge and corner bins in figure 6a and d). The range in variability between surface and interior BSP bins is also reflected in the latitude-depth plots (figure 6c and f), where deep bins have lower variability than surface bins. Latitude-longitude co-ordinates (which are depth-integrated) tend to have a smaller range in variability overall (figure 6b and e).

The difference in variability between different BSP bins, and between co-ordinate systems, can be traced to two possible sources. First, the process of integrating over the ocean volume in different co-ordinate systems may lead to differing phase-cancellation characteristics of variability that varies in space. For example, any modes of variability that result in warming at one longitude and cooling at another longitude at the same latitude and depth will compensate each other in that given latitude-depth bin, leading to reduced variability in latitude-depth compared to the longitude-latitude coordinate where the two phases of the variability are separated.

Second, watermass-based co-ordinates exclude by construction adiabatic processes (associated with, for example, wind-driven circulation changes), which may have a higher amplitude variability. Thus, the difference between variability in $T-S$ space and its Eulerian counterparts may be due to the fact that variability in $T-S$ space is solely due to diabatic processes, while variability in Eulerian co-ordinates may be due to *both* diabatic and adiabatic processes.

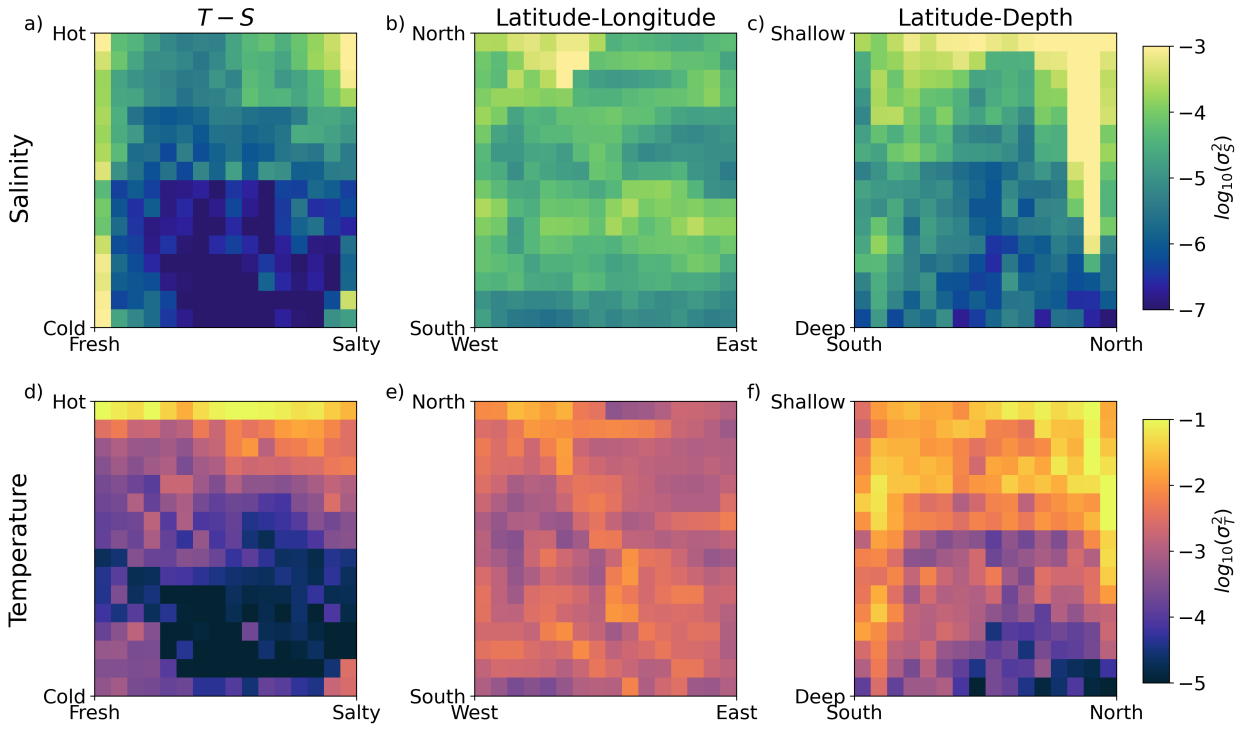

FIG. 6. (a - c) Variance in salinity, $log_{10}(\sigma_S^2)$ and (d - f) temperature, $log_{10}(\sigma_T^2)$ in equal-volume BSP bins, in (a and d) $T-S$, (b and e) latitude-longitude, and (c and f) latitude-depth co-ordinates.

The histogram of salinity and temperature variance in each co-ordinate system (figure 7) provides further insight into differences between watermass-based and Eulerian co-ordinate systems. $T-S$ co-ordinates filter out the adiabatic processes, resulting in a lower median variability, while latitude-depth and latitude-longitude both have higher median variances. The shape of the variance distributions is also instructive - both $T-S$ and latitude-depth co-ordinates have skewed distributions with long tails. Latitude-longitude co-ordinates, on the other hand, exhibit a quasi-'Normal' Gaussian distribution. This may be an interesting example of the central limit theorem, which states that statistics of random, independent variables, when summed up, are distributed with a Normal, Gaussian distribution. The process of depth-integrating may resemble such a summation of random variables (though we acknowledge that ocean processes are of course not independent) potentially leading to the Normal distribution in blue in figure 7.

As discussed in section 1, moving from one-dimensional temperature co-ordinates to two-dimensional $T-S$ co-ordinates can enable a cleaner separation of surface and ocean interior watermasses due to the addition of the salinity co-ordinate. The histograms in figure 7 indicate

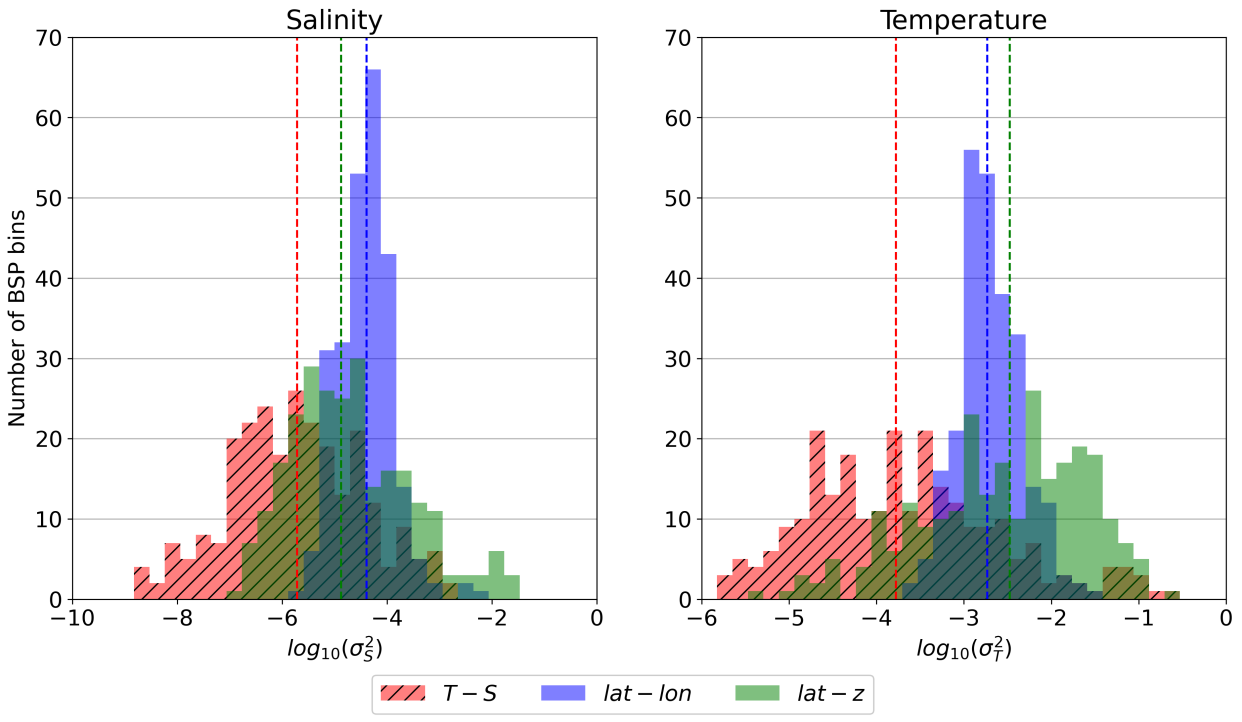

FIG. 7. Distribution of a) salinity variance, $log_{10}(\sigma_S^2)$ and b) temperature variance, $log_{10}(\sigma_T^2)$ across all BSP bins in $T-S$ (red), latitude-longitude (blue) and latitude-depth (green) co-ordinates. Dashed lines show the median variance for each co-ordinate system.

that this separation leads to a more skewed distribution of variance, with a large number of weakly varying interior bins and a small handful of surface ocean bins. Due to this skewness, the mean variance across the entire distribution (as calculated in the 1D case in Holmes et al. (2022)) for our 2D case is strongly impacted by surface bins (which have higher variance). On the other hand, the median variance (vertical lines in Fig. 7) is weaker, reflecting the much more numerous interior BSP bins. This difference is also reflected in figure A1 in the Appendix, which compares the mean and median variance across the three co-ordinate systems with different BSP slicing combinations. While the mean variance jumps around due to changes in outliers, the median variance is remarkably stable, with $T-S$ co-ordinates having a lower median variance across all plausible BSP split combinations compared to Eulerian co-ordinates (see the Appendix for details). In this work, we opt to compare the median terms of interest moving forward, though we do explore the difference between mean and median variance in our spectral analysis below.

The internal variability in figure 6 is a consequence of inter-annual and sub-decadal ocean processes, (<10 year periods, such as the El-Niño Southern Oscillation and North Atlantic Oscillation), and multi-decadal and centennial processes (>10 year periods, such as Atlantic Meridional Overturning Circulation variability). In order to parse the relative influence of sub-decadal processes on internal variability, we present the variability of the 10-year low-pass filtered temperature and salinity signal (subtracted from the total temperature and salinity variability) relative to the total temperature and salinity variability, in figure 8. A fraction of 1 in figure 8 indicates that all of the variability in the given bin may be attributed to sub-decadal processes, while a fraction of 0 indicates that all of the variability in the given bin may be attributed to multi-decadal processes. Overall, variability in $T-S$ coordinates is influenced most by multi-decadal processes (figure 8a and d). Surface waters (edge bins in figure 8a and d) have the highest proportion of sub-decadal variability in $T-S$ space. Latitude-longitude co-ordinates have a higher fraction of sub-decadal variability, particularly in the North Atlantic and Equatorial Pacific (possibly due to the influence of ENSO; figure 8b and e). Latitude-depth co-ordinates have the highest fraction of sub-decadal variability of the three co-ordinate systems. This may be due to zonally-integrated barotropic heave processes occurring at sub-decadal timescales and enhancing variability throughout the ocean column (Häkkinen et al. 2016).

The stark difference between different co-ordinate systems is highlighted by plotting the distribution of proportion of sub-decadal variance in the three co-ordinate systems explored (see figure 9). Approximately 75% of the total variability in $T-S$ space comes from > 10 year processes (red dashed lines in figure 9), suggesting that diabatic processes tend to occur, on average, at multi-decadal timescales. In contrast, around 50% (30%) of the total salinity (temperature) variability in latitude-longitude space comes from > 10 year processes (blue dashed lines in figure 9), while less than 10% of the total variability in latitude-depth space comes from > 10 year processes (green dashed lines in figure 9). These results are consistent with the one-dimensional analysis of Holmes et al. (2022) who showed that the mean temperature variance in a 1D temperature-based coordinate became comparable to variability in one-dimensional depth and latitude co-ordinates at decadal to multi-decadal time-scales, where diabatic processes dominate.

The variability fractions presented here are stable across all feasible BSP split combinations (figure A1). For all split combinations, a lower fraction of variability comes from sub-decadal

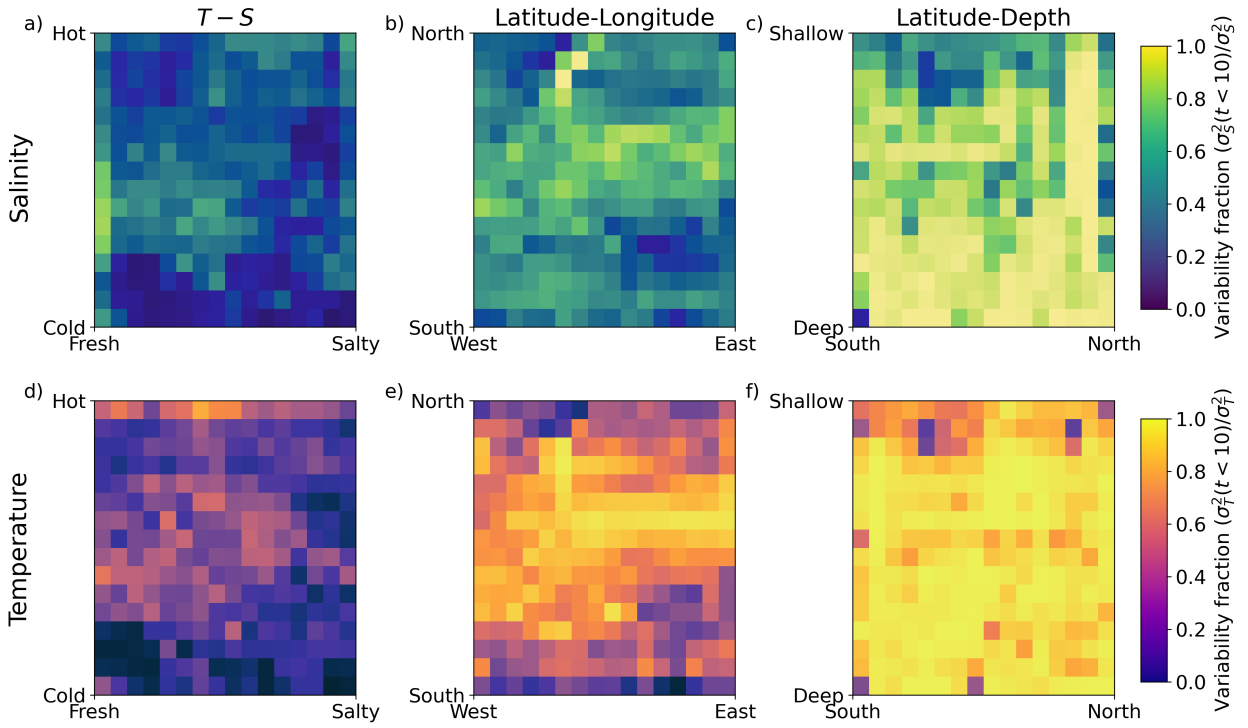

FIG. 8. Proportion of variance due to sub-decadal processes, (a - c) in salinity $\sigma_S^2(t<10)/\sigma_S^2$ and (d - f) in temperature $\sigma_T^2(t<10)/\sigma_T^2$, in (a and d) $T-S$, (b and e) latitude-longitude, and (c and f) latitude-depth co-ordinates.

processes in $T-S$ co-ordinates compared with Eulerian co-ordinates. These results provide firm evidence that $T-S$ coordinate systems capture more long-timescale flow processes than their Eulerian counterparts.

The variability in all three co-ordinate systems may be further broken down into characteristic timescales using spectral analysis, as shown in figure 10. As highlighted earlier, mean variance is more sensitive to outlier values in $T-S$ and latitude-depth space (which tend to have a skewed variance distribution). As a consequence, mean power spectra (figure 10a and c) are more impacted by outlier (often surface) sources of variability. Our mean results in figure 10c compare with the prior one-dimensional analysis of Holmes et al. (2022) (specifically, figure 11a in Holmes et al. (2022)). The mean power spectra of temperature shows a clear peak in the 2 - 3 year time period in temperature in both $T-S$ co-ordinates and latitude-longitude co-ordinates (compare blue and red lines in figure 10c), aligning with findings by Holmes et al. (2022), who concluded that this peak is likely due to ENSO. Holmes et al. (2022) found that the mean temperature variability in T space

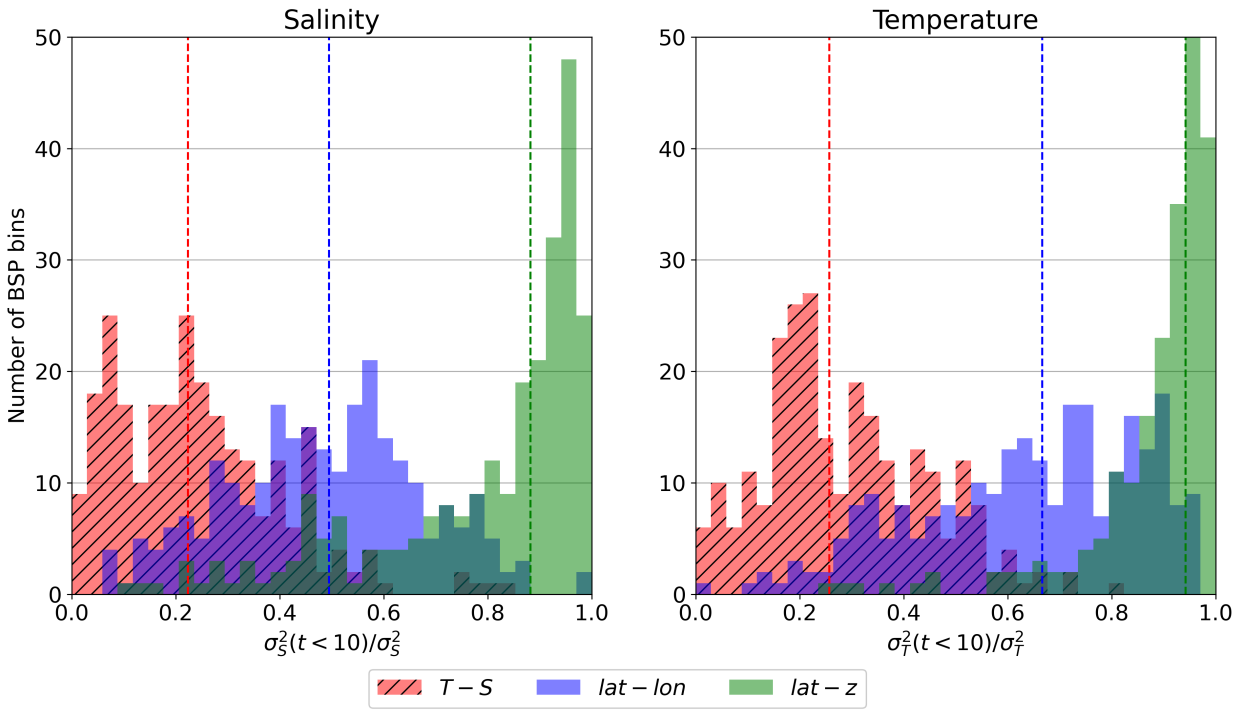

FIG. 9. Distribution of proportion of variance due to sub-decadal processes a) in salinity $\sigma_S^2(t<10)/\sigma_S^2$ and b) in temperature $\sigma_T^2(t<10)/\sigma_T^2$ across all BSP bins in $T-S$ (red), latitude-longitude (blue) and latitude-depth (green) co-ordinates. Dashed lines show the median variance proportion for each co-ordinate system.

exceeds that in depth space at $t > 10$ years. This crossover point (compare green and red lines in figure 10c) is earlier in our results due to the addition of second axes (salinity and latitude) in our analysis.

The median power spectra, a means of comparison between co-ordinate systems which is more reflective of the more numerous ocean interior bins, show a stark difference between variance in Eulerian and watermass-based co-ordinates (figures 10b and d). Across all time periods, median variance in $T-S$ space is lower than that in latitude-longitude or latitude-depth space. The difference between sub-decadal and multi-decadal variability is also most pronounced in $T-S$ space, re-enforcing findings in figure 9. Overall, latitude-longitude co-ordinates have the highest median variance across most time periods, though temperature variances are similar in latitude-longitude and latitude-depth space (figure 10d; compare green and blue lines).

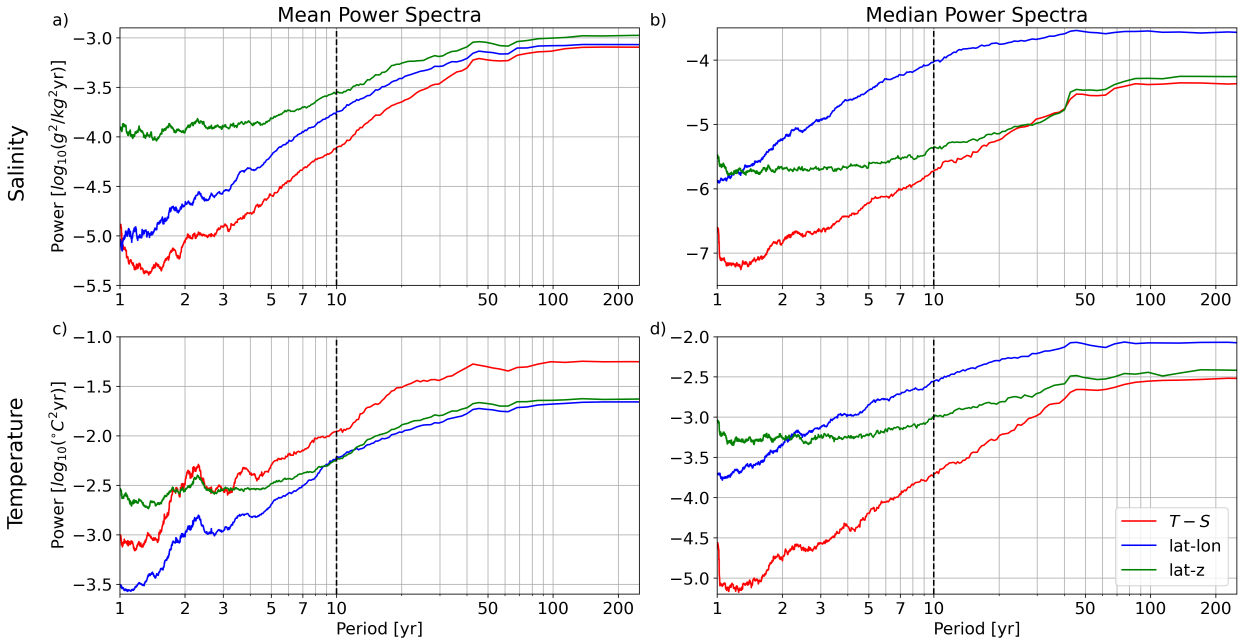

FIG. 10. Power spectra of (a and b) salinity variability and (c and d) temperature variability in $T-S$ co-ordinates (red), latitude-longitude co-ordinates (blue) and latitude-depth co-ordinates (green). Spectra are presented both as the mean of all BSP bins (a and c) and the median of all BSP bins (b and d). The vertical dashed line shows a period of 10 years, the cutoff used in figure 8. Power spectra are calculated from monthly data, using Thompson's multitaper method with 19 Slepian tapers.

b. Modes of Variability

The primary modes of variability that drive internal variability in the three coordinate systems may be explored via Principal Component Analysis (PCA), where a principal component (PC) is the eigenvector of the covariance matrix of the distribution. The correlation coefficients obtained from PCA can indicate dominant modes of variability in the time series. PCA yields several PCs which collectively explain the total variance in a time series. We can thus find the number of PCs needed to adequately explain a high proportion of variance in a time series – the lower the number of PCs, the 'simpler' the time series can be considered to be. Figure 11 shows the cumulative proportion of variance explained by the PCs obtained from PCA.

$T-S$ space captures total temperature and salinity variance with the fewest principal components. The difference between $T-S$ and its Eulerian components is particularly large when assessing temperature variability, as shown in figure 11a. In $T-S$ space, 95% of the total temperature

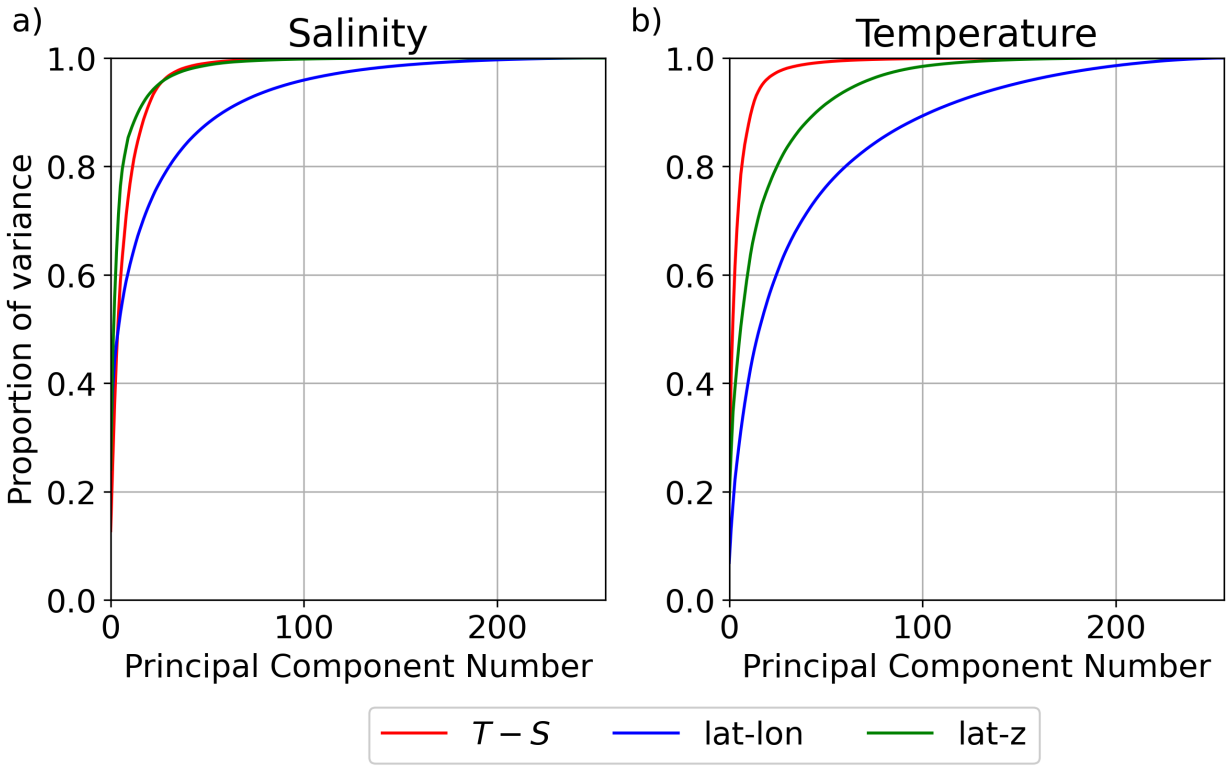

FIG. 11. Cumulative proportion of total variance captured by principal components in the Principal Component Analysis, for monthly a) salinity, and b) temperature, in $T-S$ co-ordinates (red), latitude-longitude co-ordinates (blue) and latitude-depth co-ordinates (green).

variance is captured in 17 principal components, while in latitude-depth and latitude-longitude co-ordinates 67 and 146 PCs respectively are required to capture 95% of temperature variance.

The difference between water-mass coordinates and Eulerian coordinates is less distinct in the salinity time series (figure 11b). 95% of salinity variance can be captured by 26, 25, and 91 PCs in $T-S$ space, latitude-depth space and latitude-longitude space, respectively. Thus, while $T-S$ co-ordinates remain the preferred choice to express temperature variability most simply, latitude-depth presents an equivalent alternative for salinity variability.

5. Discussion: Implications for signal-to-noise ratio

Overall, our results show that the projection of internal variability, or 'noise' in the climate system, into $T-S$ co-ordinates is reduced compared to Eulerian frameworks. In theory, this should mean that the historical signal of ocean heating and salinity change should emerge from background

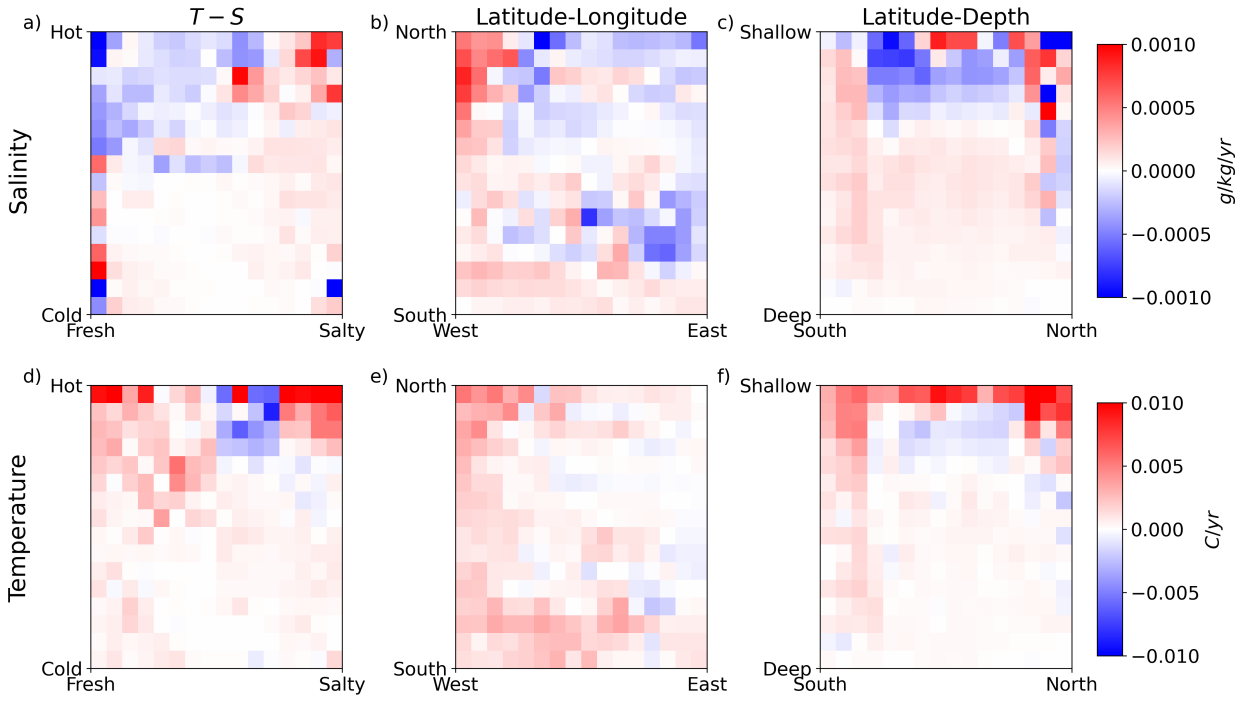

FIG. 12. Linear trend in historical (a - c) salinity (in g/kg/year) and (d - f) temperature (in °C/year), in (a and d) $T-S$, (b and e) latitude-longitude, and (c and f) latitude-depth co-ordinates, from 1970-2014. The linear trend is calculated by finding the slope of the linear regression on monthly data from January 1970 to December 2014.

variability more cleanly in $T-S$ space, manifesting as a higher median signal-to-noise ratio. Here we assess the 'signal', that is, the historical temperature and salinity tendency, in $T-S$, latitude-depth space and latitude-longitude space. Figure 12 shows the temperature and salinity tendencies from 1970 to 2014 in the ACCESS-CM2 historical simulations. The salinity tendency (figure 12a, b and c) aligns with previous model and historical estimates of salt content change. In $T-S$ space, salty regions get saltier, and fresh regions get fresher, following a 'wet-gets-wetter-dry-gets-drier' pattern (Allan et al. 2020). Overall, the changes in salinity in $T-S$ space and latitude-depth space align with findings by (Sohail et al. 2022; Silvy et al. 2020).

Temperature tendency in a fixed-volume framework is proportional to heat content change, so the temperature tendencies presented in figure 12d, e and f may be though of as equivalent to the ocean heat content change. In $T-S$ space, there is broad warming over almost all water masses, save a small water mass in a warm, salty quadrant of the global ocean. This warming profile is consistent, at least in temperature space and depth space, with findings by Sohail et al. (2021).

Thus, the BSP remapping captures well previously observed trends in ocean heat and salt content, lending credence to the method as a means to assess changes in historical temperature and salinity, or the climate change 'signal'.

Having quantified both the temperature and salinity signal and noise in the climate system, we proceed to test whether $T-S$ co-ordinates do indeed improve the signal-to-noise ratio compared to more traditional Eulerian frameworks. We focus on the entire historical signal, from 1850 to 2014, as our climate 'signal. We follow equation (1) to calculate signal-to-noise ratio, and use the end-to-end difference over the historical period (i.e., C in 2014 minus C in 1850) as ΔC in the signal-to-noise ratio calculation. The signal-to-noise ratio in $T-S$, latitude-depth and latitude-longitude space is shown for each BSP bin in figure 13, for salinity (panels a-c), and temperature (panels d-f). $T-S$ coordinates broadly show the highest signal-to-noise ratio, with a large proportion of bins having a signal which exceeds twice the standard deviation of the pre-industrial control simulations $F/N > 2$. Latitude-depth coordinates perform relatively well in isolating the forced signal in salinity space, particularly in the deep ocean, with higher signal-to-noise ratio values in this region. However, this trend is not replicated for temperature. Latitude-longitude coordinates perform the worst in isolating the historical forced signal from internal variability, with the vast majority of bins having a relatively low signal-to-noise ratio, in both salinity and temperature.

The difference in signal-to-noise ratio between the three co-ordinate systems is well illustrated in histograms of the signal-to-noise ratio, shown in figure 14. $T-S$ co-ordinates exhibit a much longer tail of high signal-to-noise ratios compared with their Eulerian counterparts. Note that the difference between mean and median for these signal-to-noise ratio results (i.e. the skewness of the signal-to-noise histogram) is much less extreme than for the raw variance comparison, precisely because the signal, in addition to the 'noise', is strongly skewed toward the surface. As a consequence, the mean and median signal-to-noise ratio in $T-S$ co-ordinates is consistently higher than in Eulerian co-ordinates. The median (mean) signal-to-noise ratio for salinity is 4.7 (5.2) for $T-S$, compared with 1.6 (1.9) and 2.5 (3.2) for latitude-longitude and latitude-depth, respectively. The median (mean) signal-to-noise ratio for temperature is 4.3 (5.1) for $T-S$, compared with 1.6 (1.8) and 1.4 (1.5) for latitude-longitude and latitude-depth, respectively. Thus, these results indicate that two-dimensional watermass co-ordinates are at least 2 times better at isolating the

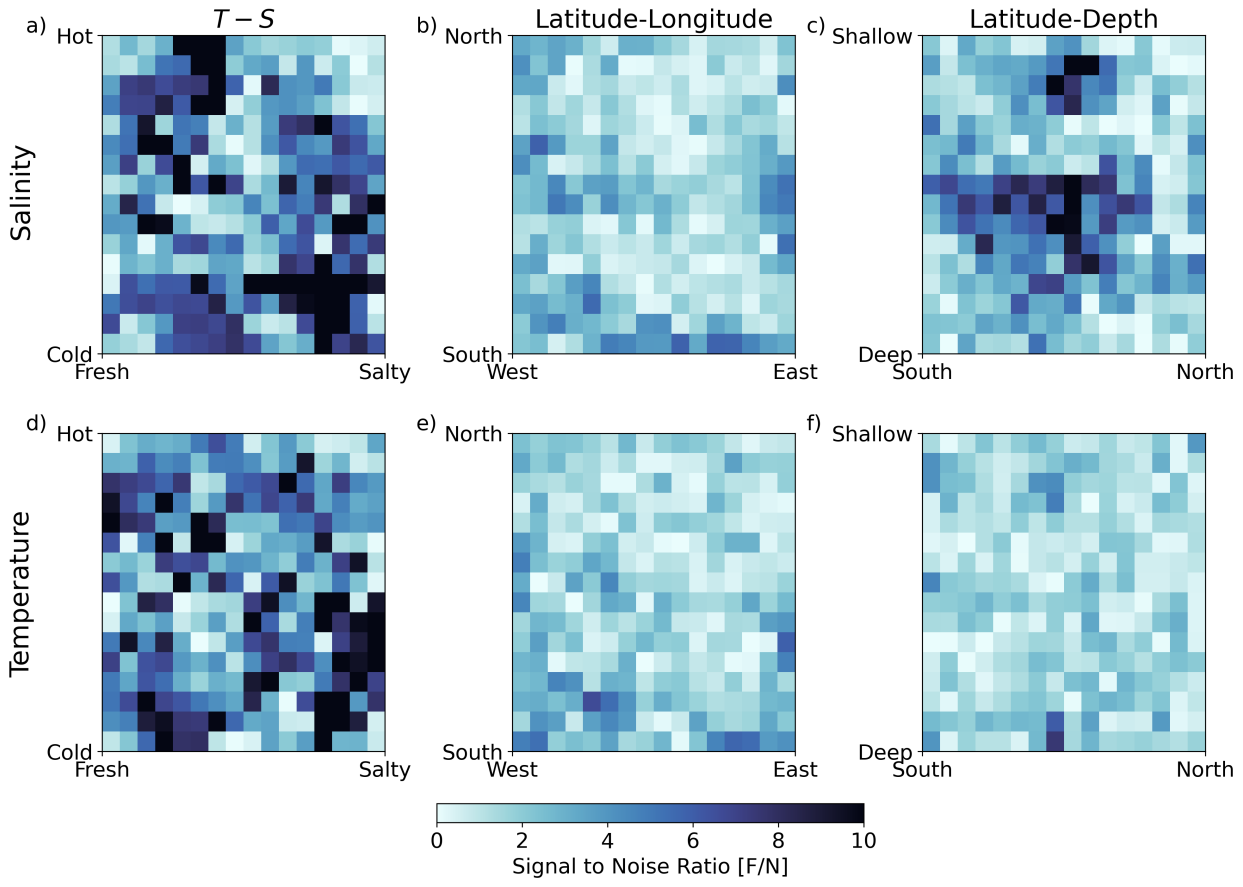

FIG. 13. Signal-to-noise ratio of (a - c) salinity and (d - f) temperature, in (a and d) $T-S$, (b and e) latitude-longitude, and (c and f) latitude-depth co-ordinates.

forced temperature and salinity signal from background variability based on their signal-to-noise ratio.

There are several questions open for further exploration, particularly in terms of the BSP algorithm presented here. In the past, watermass-based frameworks have been used to develop simple ocean heat and salt content budgets, wherein salt and heat content tendencies can be related solely to diabatic air-sea flux and mixing processes (Holmes et al. 2019; Sohail et al. 2021; Bladwell et al. 2021). In the two-dimensional BSP framework, such a budget is more difficult to formulate, as changes to the properties of a bin can potentially change the BSP bins in adjacent $T-S$ regions. That said, the formulation of a budget in the BSP framework may still yield new insights into ocean dynamics, and is reserved for future analysis.

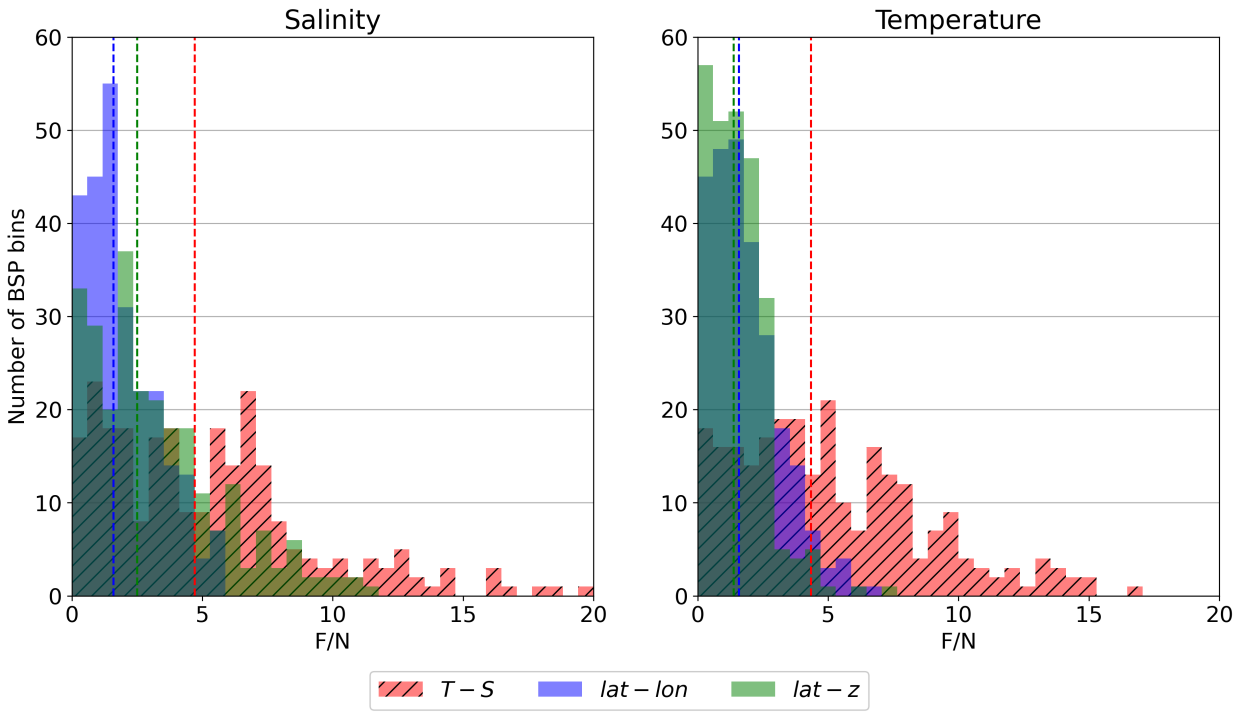

456 FIG. 14. Frequency of occurrence of each signal-to-noise ratio in BSP bins, for a) salinity and b) temperature, in
457 $T-S$ co-ordinates (red), latitude-longitude co-ordinates (blue) and latitude-depth co-ordinates (green). Vertical
458 dashed lines show the median signal-to-noise ratio for each co-ordinate system.

467 In addition, one-dimensional analyses in temperature space have highlighted the potential benefits
468 of using watermass-based co-ordinates to reduce sampling bias arising from adiabatic heave in
469 observations (Palmer et al. 2007; Palmer and Haines 2009). BSP presents an opportunity to extract
470 synthetic profiles from climate model data, following Allison et al. (2019), and assess the influence
471 of two-dimensional co-ordinate systems on observational sampling biases and observed heat and
472 salt content.

473 6. Conclusions

474 Watermass-based frameworks are becoming popular for capturing changes in ocean heat and
475 salt content, in part because they are believed to reduce internal variability, thus more effectively
476 isolating the historical 'signal' of climate change. However, a rigorous comparison between
477 watermass-based frameworks and Eulerian (latitude-longitude, latitude-depth, etc.) co-ordinate
478 systems has been difficult due to fundamental differences in the way these co-ordinate systems

are formulated. In this work, we introduce a statistical method, called *Binary Space Partitioning* (BSP) to recast $T-S$, latitude-longitude and latitude-depth co-ordinate systems onto an equivalent, equal-volume co-ordinate. Applied to pre-industrial control and historical simulations of a state-of-the-art climate model, ACCESS-CM2, BSP enables an apples-to-apples comparison of internal variability between watermass-based and Eulerian co-ordinates. We find that $T-S$ co-ordinates isolate the climate change signal such that median variability is reduced, and the majority of the variability that *is* captured can be attributed to multi-decadal processes in this framework. With a reduced 'noise' component, the historical signal is shown to be more effectively isolated in $T-S$ space, with a signal-to-noise ratio that is at least two times greater than its Eulerian counterparts. Thus, we conclusively show that watermass-based co-ordinates isolate the historical climate change signal more effectively than latitude-longitude and latitude-depth co-ordinates.

Acknowledgments. We acknowledge the World Climate Research Programme (WCRP), the CMIP6 climate modeling groups for producing and making available their model output, and the Earth System Grid Federation (ESGF) as well as the funding agencies which support the WCRP, CMIP6 and ESGF. All data analysis was conducted at facilities which form part of the National Computational Infrastructure (NCI), which is supported by the Commonwealth of Australia. The authors are supported by the Australian Research Council (ARC) Centre of Excellence for Climate Extremes, the Australian Centre for Excellence in Antarctic Science (ACEAS), and the ARC Discovery Project scheme DP190101173. We acknowledge support from ARC award DE21010004. We thank Dr. John A. Church for assistance in the interpretation of results.

Data availability statement. All data used in this work is publicly available via ESGF: https://esgf-node.llnl.gov/search/cmip6/.

APPENDIX A

Variability across 2^n combinations of axis subdivisions

In this study, we opt to subdivide alternating axes (starting with the $y-$axis) 8 times, to yield $2^8 = 256$ bins. However, as mentioned in section 3, there are 256 possible combinations of axis subdivisions that may have been chosen, including $xxxxxxxx$, $xxxxxxy$, $yyyyyyyx$, etc. In

this appendix, we explore the influence of choosing some of these other combinations of axis subdivisions on our results.

When assessing internal variability in two-dimensional tracer space, an ideal coordinate system would equally represent changes in both the $x-$ and $y-$axes. For instance, in some climate model grids latitude and longitude have roughly equivalent resolutions as variability in the latitudinal and longitudinal directions is roughly similar. Of course, for the sake of reducing computational complexity, dimensions which are known apriori to exhibit characteristically lower variability may have reduced resolution - for instance, ocean model grids typically have lower depth resolution than latitude or longitude. Without such apriori knowledge of variability in a given dimension, and in an attempt to create a like-for-like co-ordinate system, we argue that the most appropriate BSP split combinations would be ones that preserve the aspect ratio of bins. Thus, we propose that the most physically plausible BSP split combinations are combinations of xy and yx. Always splitting in axis pairs ensures that no long, thin bins are created which span a large range in one dimension but a small range in another dimension.

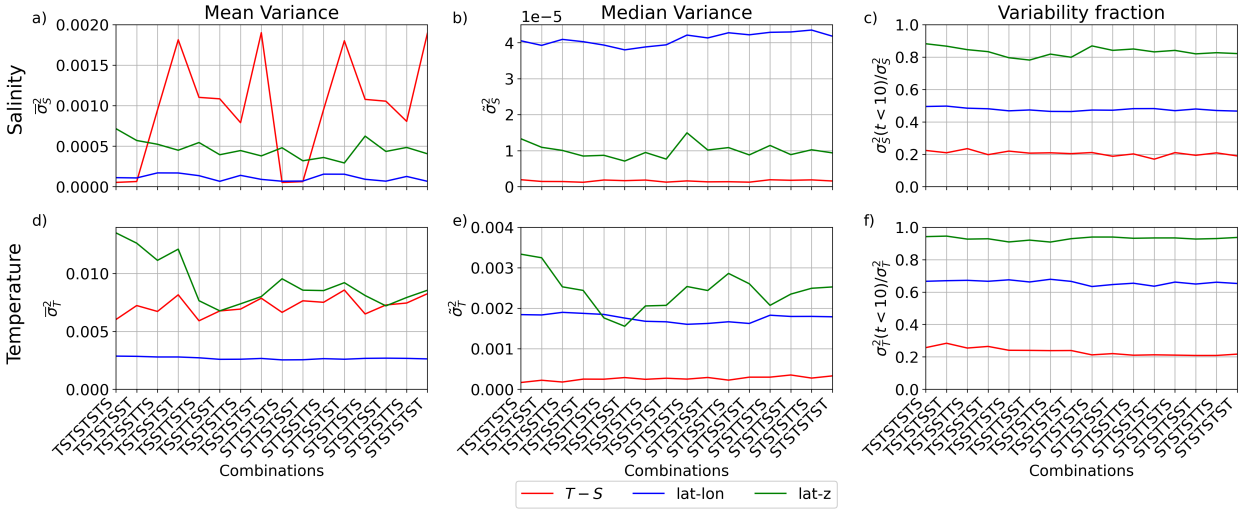

FIG. A1. (a and d) Mean and (b and e) Median variance, and (c and f) Median fraction of sub-decadal variance in $T - S$ (red), latitude-longitude (blue) and latitude-depth (green) co-ordinates across 16 plausible BSP split combinations.

For $n = 8$, there are 16 yx and xy combinations that preserve the BSP bin aspect ratio. The mean temperature and salinity variance changes across across the 16 combinations of BSP slices (figure A1a and d, where $S = x$ and $T = y$). As mentioned in section 4, this is because the distribution of variance in $T - S$ and latitude-depth space is highly skewed, meaning outliers have an outsized role in modifying the mean variance across all BSP bins. Instead, looking at median variance (figure A1b and e) shows a much more consistent picture, with $T - S$ co-ordinates having a lower variance across all split combinations. The median variance fraction (figure A1c and f) shows a similarly consistent picture. Across all BSP split combinations, $T - S$ co-ordinates are dominated by multi-decadal processes, while latitude-depth co-ordinates are dominated by sub-decadal processes. Our exploration of alternative BSP split combinations further solidifies our findings, summarised in section 6, showing that reduced variance in watermass-based frameworks is insensitive to the order of BSP splitting used.

APPENDIX B

Geographic location of watermasses in $T - S$ space

It is difficult to conceptualise changes in watermass space in terms of the geographic location of said water masses. In an attempt to aid in interpretation of the results we show the volume fraction in each latitude-longitude and latitude-depth grid cell that corresponds to the warmest (coldest) and freshest (saltiest) 25% volume of the ocean, in figure B1. The 25% coldest and freshest ocean by volume is predominantly located in the Southern Ocean and surface Arctic ocean (figure B1a, b and c). Antarctic Bottom Water and Pacific subsurface waters are captured in this quadrant. The 25% coldest and saltiest ocean is much more broadly distributed - and largely corresponds to the deepest ocean water (figure B1d, e and f). The North Atlantic Deep Water and North Atlantic overturning are captured in this quadrant.

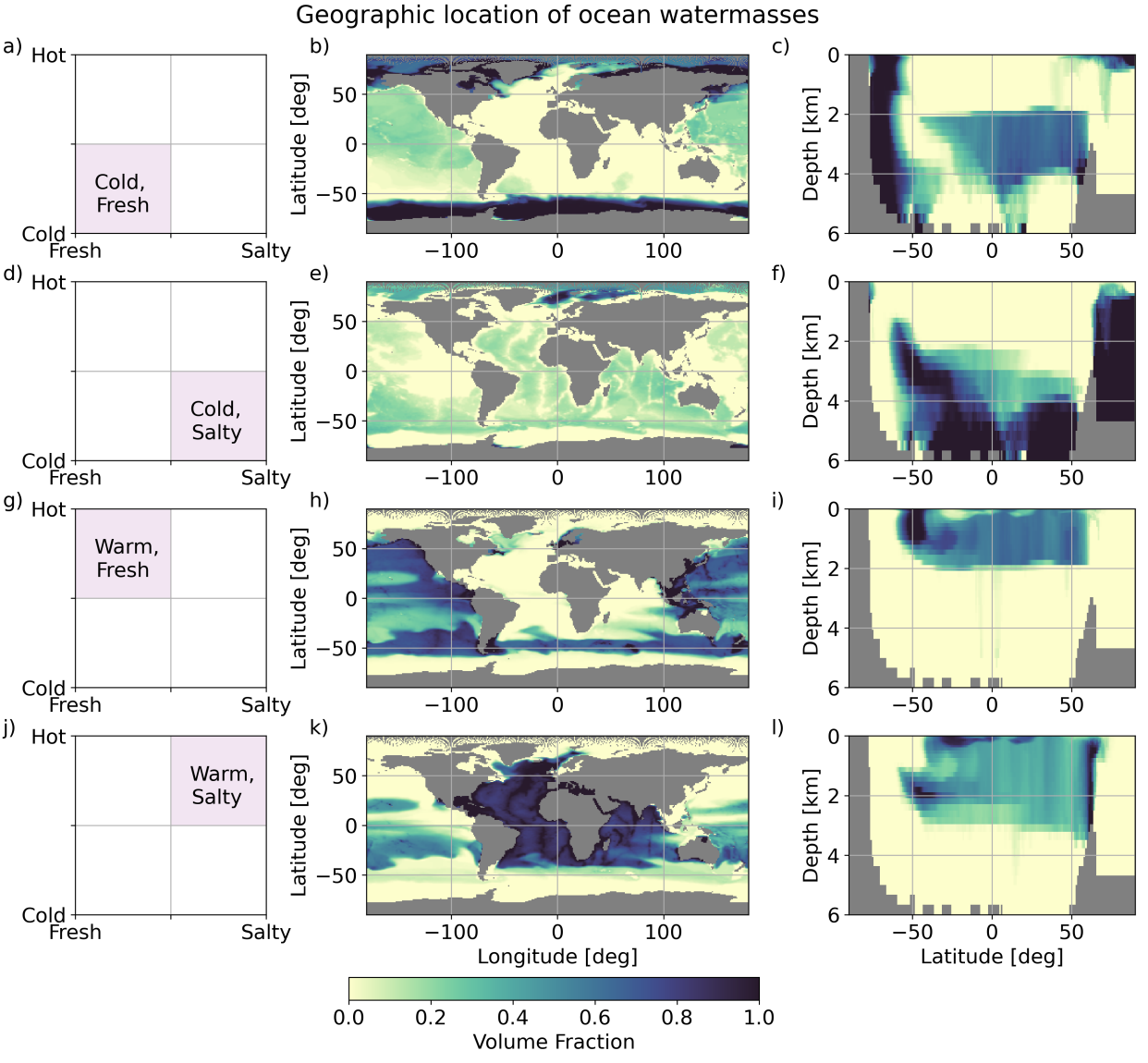

FIG. B1. The volume fraction, in latitude-longitude and latitude-depth co-ordinates, occupied by four water masses in $T-S$ space: (a, b and c) The coldest, freshest 25% of the ocean, (d, e and f) the coldest, saltiest 25% of the ocean, (g, h and i) the warmest, freshest 25% of the ocean and (j, k and l) the warmest, saltiest 25% of the ocean. Land masses are marked in grey.

The 25% warmest and freshest ocean is largely isolated to the surface Pacific ocean, as well as the Antarctic Intermediate Water, but excludes the Pacific subpolar gyres (figure B1g, h and i). The 25% warmest and saltiest ocean, on the other hand, is almost exclusively isolated to the Indian and Atlantic oceans (excluding the Indo-Pacific warm pool), and includes the Pacific subpolar gyres (figure B1j, k and l).

References

Allan, R. P., and Coauthors, 2020: Advances in understanding large-scale responses of the water cycle to climate change. *Annals of the New York Academy of Sciences*, **1472 (1)**, 49–75, https://doi.org/10.1111/nyas.14337.

Allison, L. C., C. D. Roberts, M. D. Palmer, L. Hermanson, R. E. Killick, N. A. Rayner, D. M. Smith, and M. B. Andrews, 2019: Towards quantifying uncertainty in ocean heat content changes using synthetic profiles. *Environmental Research Letters*, **14 (8)**, 084 037, https://doi.org/10.1088/1748-9326/ab2b0b.

Bi, D., and Coauthors, 2020: Configuration and spin-up of ACCESS-CM2, the new generation Australian Community Climate and Earth System Simulator Coupled Model. *Journal of Southern Hemisphere Earth Systems Science*, https://doi.org/10.1071/es19040.

Bladwell, C., R. M. Holmes, and J. D. Zika, 2021: Internal salt content: a useful framework for understanding the oceanic branch of the water cycle. *Journal of Physical Oceanography*, https://doi.org/10.1175/jpo-d-20-0212.1.

Boyer, T. P., S. Levitus, J. I. Antonov, R. A. Locarnini, and H. E. Garcia, 2005: Linear trends in salinity for the World Ocean, 1955–1998. *Geophysical Research Letters*, **32 (1)**, https://doi.org/10.1029/2004gl021791.

Durack, P. J., S. E. Wijffels, and R. J. Matear, 2012: Ocean Salinities Reveal Strong Global Water Cycle Intensification During 1950 to 2000. *Science*, **336 (6080)**, 455–458, https://doi.org/10.1126/science.1212222.

Evans, D. G., J. D. Zika, A. C. N. Garabato, and A. J. G. Nurser, 2014: The imprint of Southern Ocean overturning on seasonal water mass variability in Drake Passage. *Journal of Geophysical Research: Oceans*, **119 (11)**, 7987–8010, https://doi.org/10.1002/2014jc010097.

Eyring, V., S. Bony, G. A. Meehl, C. A. Senior, B. Stevens, R. J. Stouffer, and K. E. Taylor, 2016: Overview of the Coupled Model Intercomparison Project Phase 6 (CMIP6) experimental design and organization. *Geoscientific Model Development*, **9 (5)**, 1937–1958, https://doi.org/10.5194/gmd-9-1937-2016.

Griffies, S. M., 2012: Elements of the Modular Ocean Model (MOM). *GFDL Ocean Group Tech. Rep.*, **7**, 620.

Groeskamp, S., P. M. Barker, T. J. McDougall, R. P. Abernathey, and S. M. Griffies, 2019: VENM: An Algorithm to Accurately Calculate Neutral Slopes and Gradients. *Journal of Advances in Modeling Earth Systems*, **11 (7)**, 1917–1939, https://doi.org/10.1029/2019ms001613.

Hamlington, B. D., R. R. Leben, R. S. Nerem, and K.-Y. Kim, 2011: The Effect of Signal-to-Noise Ratio on the Study of Sea Level Trends. *Journal of Climate*, **24 (5)**, 1396–1408, https://doi.org/10.1175/2010jcli3531.1.

Hawkins, E., and R. Sutton, 2012: Time of emergence of climate signals. *Geophysical Research Letters*, **39 (1)**, n/a–n/a, https://doi.org/10.1029/2011gl050087.

Hieronymus, M., J. Nilsson, and J. Nycander, 2014: Water Mass Transformation in Salinity–Temperature Space. *Journal of Physical Oceanography*, **44 (9)**, 2547–2568, https://doi.org/10.1175/jpo-d-13-0257.1.

Holmes, R. M., T. Sohail, and J. D. Zika, 2022: Adiabatic and Diabatic Signatures of Ocean Temperature Variability. *Journal of Climate*, **35 (5)**, 1459–1477, https://doi.org/10.1175/jcli-d-21-0695.1.

Holmes, R. M., J. D. Zika, and M. H. England, 2019: Diathermal Heat Transport in a Global Ocean Model. *Journal of Physical Oceanography*, **49 (1)**, 141–161, https://doi.org/10.1175/jpo-d-18-0098.1.

Häkkinen, S., P. B. Rhines, and D. L. Worthen, 2016: Warming of the global ocean: spatial structure and water-mass trends. *Journal of Climate*, **29 (13)**, 4949–4963, https://doi.org/10.1175/jcli-d-15-0607.1.

Irving, D., W. Hobbs, J. Church, and J. Zika, 2020: A Mass and Energy Conservation Analysis of Drift in the CMIP6 Ensemble. *Journal of Climate*, **34 (8)**, 3157–3170, https://doi.org/10.1175/jcli-d-20-0281.1.

Maher, N., S. Milinski, and R. Ludwig, 2021: Large ensemble climate model simulations: introduction, overview, and future prospects for utilising multiple types of large ensemble. *Earth System Dynamics*, **12 (2)**, 401–418, https://doi.org/10.5194/esd-12-401-2021.

McDougall, T. J., 2003: Potential Enthalpy: A Conservative Oceanic Variable for Evaluating Heat Content and Heat Fluxes. *Journal of Physical Oceanography*, **33 (5)**, 945–963, https://doi.org/10.1175/1520-0485(2003)033<0945:peacov>2.0.co;2.

McDougall, T. J., and P. M. Barker, 2011: Getting started with TEOS---10 and the Gibbs Seawater (GSW) Oceanographic Toolbox. *SCOR/IAPSO WG127*, 28.

Morrison, A. K., and A. M. Hogg, 2013: On the Relationship between Southern Ocean Overturning and ACC Transport. *Journal of Physical Oceanography*, **43 (1)**, 140–148, https://doi.org/10.1175/jpo-d-12-057.1.

Palmer, M. D., and K. Haines, 2009: Estimating Oceanic Heat Content Change Using Isotherms. *Journal of Climate*, **22 (19)**, 4953–4969, https://doi.org/10.1175/2009jcli2823.1.

Palmer, M. D., K. Haines, S. F. B. Tett, and T. J. Ansell, 2007: Isolating the signal of ocean global warming. *Geophysical Research Letters*, **34 (23)**, n/a–n/a, https://doi.org/10.1029/2007gl031712.

Penland, C., and L. Matrosova, 2006: Studies of El Niño and Interdecadal Variability in Tropical Sea Surface Temperatures Using a Nonnormal Filter. *Journal of Climate*, https://doi.org/https://doi.org/10.1175/JCLI3951.1.

Pierce, D. W., P. J. Gleckler, T. P. Barnett, B. D. Santer, and P. J. Durack, 2012: The fingerprint of human-induced changes in the ocean's salinity and temperature fields. *Geophysical Research Letters*, **39 (21)**, n/a–n/a, https://doi.org/10.1029/2012gl053389.

Radha, H., M. Vetterli, and R. Leonardi, 1996: Image compression using binary space partitioning trees. *IEEE Transactions on Image Processing*, **5 (12)**, 1610–1624, https://doi.org/10.1109/83.544569.

Rathore, S., N. L. Bindoff, H. E. Phillips, and M. Feng, 2020: Recent hemispheric asymmetry in global ocean warming induced by climate change and internal variability. *Nature Communications*, **11 (1)**, 2008, https://doi.org/10.1038/s41467-020-15754-3.

Roemmich, D., J. Church, J. Gilson, D. Monselesan, P. Sutton, and S. Wijffels, 2015: Unabated planetary warming and its ocean structure since 2006. *Nature Climate Change*, **5 (3)**, 240–245, https://doi.org/10.1038/nclimate2513.

Schuckmann, K. v., and Coauthors, 2020: Heat stored in the Earth system: where does the energy go? *Earth System Science Data*, **12 (3)**, 2013–2041, https://doi.org/10.5194/essd-12-2013-2020.

Silvy, Y., E. Guilyardi, J.-B. Sallée, and P. J. Durack, 2020: Human-induced changes to the global ocean water masses and their time of emergence. *Nature Climate Change*, 1–7, https://doi.org/10.1038/s41558-020-0878-x.

Sohail, T., D. B. Irving, J. D. Zika, R. M. Holmes, and J. A. Church, 2021: Fifty Year Trends in Global Ocean Heat Content Traced to Surface Heat Fluxes in the Sub-Polar Ocean. *Geophysical Research Letters*, **48 (e2020GL091439)**, 1 – 13, https://doi.org/10.1029/2020gl091439.

Sohail, T., J. D. Zika, D. B. Irving, and J. A. Church, 2022: Observed poleward freshwater transport since 1970. *Nature*, **602 (7898)**, 617–622, https://doi.org/10.1038/s41586-021-04370-w.

Stocker, and Coauthors, 2013: Climate Change 2013: The Physical Science Basis. Contribution of Working Group I to the Fifth Assessment Report of the Intergovernmental Panel on Climate Change. Tech. rep., Cambridge University Press, 1535 pp.

Thibault, W. C., and B. F. Naylor, 1987: Set operations on polyhedra using binary space partitioning trees. *ACM SIGGRAPH Computer Graphics*, **21 (4)**, 153–162, https://doi.org/10.1145/37401.37421.

Trenberth, K. E., 2020: ENSO in the global climate system. *El Nino Southern Oscillation in a Changing Climate*, Vol. 253, American Geophysical Union, 21 – 37, https://doi.org/https://doi.org/10.1002/9781119548164.ch2.

Visbeck, M. H., J. W. Hurrell, L. Polvani, and H. M. Cullen, 2001: The North Atlantic Oscillation: Past, present, and future. *Proceedings of the National Academy of Sciences*, **98 (23)**, 12 876–12 877, https://doi.org/10.1073/pnas.231391598.

Walin, G., 1982: On the relation between sea-surface heat flow and thermal circulation in the ocean. *Tellus*, **34 (2)**, 187–195, https://doi.org/10.3402/tellusa.v34i2.10801.

Wolfe, C. L., P. Cessi, J. L. McClean, and M. E. Maltrud, 2008: Vertical heat transport in eddying ocean models. *Geophysical Research Letters*, **35 (23)**, https://doi.org/10.1029/2008gl036138.

Worthington, L. V., 1981: The Water Masses of the World Ocean:Some Results of a Fine-Scale Census.

Zika, J. D., J. M. Gregory, E. L. McDonagh, A. Marzocchi, and L. Clément, 2021: Recent Water Mass Changes Reveal Mechanisms of Ocean Warming. *Journal of Climate*, **34 (9)**, 3461–3479, https://doi.org/10.1175/jcli-d-20-0355.1.

Zika, J. D., N. Skliris, A. T. Blaker, R. Marsh, A. J. G. Nurser, and S. A. Josey, 2018: Improved estimates of water cycle change from ocean salinity: the key role of ocean warming. *Environmental Research Letters*, **13 (7)**, 074 036, https://doi.org/10.1088/1748-9326/aace42.

Zika, J. D., N. Skliris, A. J. G. Nurser, S. A. Josey, L. Mudryk, F. Laliberté, and R. Marsh, 2015: Maintenance and Broadening of the Ocean's Salinity Distribution by the Water Cycle. *Journal of Climate*, **28 (24)**, 9550–9560, https://doi.org/10.1175/jcli-d-15-0273.1.